Received: 10 March 2023 | Revised: 1 July 2023 | Accepted: 26 July 2023

DOI: 10.1111/ffe.14124

ORIGINAL ARTICLE

FFEMS Fatigue & Fracture of Engineering Materials & Structures

WILEY

Study of cyclic crack-tip opening displacement of microstructurally small fatigue crack using digital image correlation

Ilari Tillikainen | **Pasquale Gallo** | **Pauli Lehto** | **Heikki Remes**

Department of Mechanical Engineering, Aalto University, Espoo, Finland

Correspondence
Pasquale Gallo, Aalto University, Department of Mechanical Engineering, Otakaari 4, 02150, Espoo, Finland.
Email: pasquale.gallo@aalto.fi

Funding information
Academy of Finland, Grant/Award Numbers: 298762, 321244; Aalto University

Abstract

The current work investigates the relationship between the crack growth rate (CGR) and the cyclic crack-tip opening displacement (ΔCTOD) of microstructurally small fatigue cracks by using high-resolution digital image correlation (DIC). Load-controlled fatigue tests were conducted on small-scale specimens of 18%Cr body-centered cubic ferritic stainless steel. Microstructurally small fatigue crack growth was analyzed based on accurate high sample-rate measurements, starting from a sub-grain crack length up to seven times the volume-weighted grain size $d_v = 224$ μm. Under these experimental conditions, the high-resolution analyses reveal that variation from the otherwise linear relationship between CGR and ΔCTOD on double logarithmic scale is due to the crack-tip bypassing an inhomogeneous shear strain localization zone. In this zone, ΔCTOD is not able to characterize the behavior of microstructurally small fatigue cracks. Outside the shear strain localization zone, ΔCTOD still is a valid crack driving force parameter.

KEYWORDS

crack growth rate, crack tip opening displacement, ferritic stainless steel, small crack, strain localization

Highlights

- Crack tip opening displacement range ΔCTOD and CGR show mostly linear relationship.
- ΔCTOD and CGR relationship becomes non-linear if shear strain accumulation is present.
- If the crack tip penetrates the hardened region, CGR decreases.
- Strain accumulation is influenced by grain orientation and grain size.

1 | INTRODUCTION

Like other industrial fields, the maritime industry has shown a clear trend of shifting towards cleaner and greener technology by seeking solutions that can lower emissions and improve the efficiency of the vessels. In this regard, weight saving achieved through lightweight designs could drastically increase fuel efficiency and provide additional payload capacity. To achieve this target, the employment of high-strength steels and thin plates is currently considered among the most promising solutions.[1–4] In this new class of resilient steel structures, often coupled with modern manufacturing methods producing components with high surface integrity, cracks may spend most of their lifetime at the microstructural level, interacting with local microstructural features. Consequently, the importance of small crack analyses has risen, since small crack propagation determines a significant part of the fatigue life in those applications. These recent new developments have brought a paradigm shift in fatigue design. Indeed, in classic fatigue strength assessment methods, the focus is mainly on cracks long compared to the microstructural scale, and thus, they do not apply to small fatigue cracks.[5] Although several modeling approaches have been presented to address small crack behavior,[6–12] there is still a clear research gap in investigating the local crack driving force, clarifying the interaction with local microstructural features, and developing models that are based on the directly measured local crack driving forces, e.g., crack-tip opening displacement (CTOD).[13]

Microstructurally small fatigue cracks propagate faster than long cracks at comparable stress intensity factor ranges (ΔK) and have different growth kinetics.[14] The propagation is primarily Stage I crack growth by shearing, either along a single crystallographic slip plane or alternating between two preferential slip planes leading to a faceted crack surface.[15,16] In the past two decades, several researchers have provided numerous insights into the physical nature of small crack growth.[17] With increasing computational capabilities, sophisticated multiscale modeling frameworks[18] and data-driven machine learning approaches[19] have been used to study the complex phenomena behind the propagation of small cracks. Still, the data-driven approaches face several challenges due to the limited availability of high-quality experimental data.[20] Consequently, microstructurally small fatigue crack growth and crack interactions with the microstructure is still an open topic due to the complex three-dimensional nature of the problem and the experimental challenges of observing the phenomena at such a small scale.[21]

The behavior of microstructurally small cracks is often investigated with a focus on the crack driving force. Commonly used parameters are, e.g., the stress intensity factor range ΔK derived from the theory of linear elastic fracture mechanics (LEFM) and J-integral. While the *effective* ΔK[22] has been used to unify the crack growth rates (CGR) of long and small cracks in some cases,[23,24] the use of a LEFM-based concept in applications where small-scale yielding and crack-tip similitude concepts are probably violated remains controversial. On the contrary, the CTOD is considered a viable alternative under these conditions.[25,26] It is well-known that ΔCTOD and CGR (da/dN) of long cracks have a linear correlation on a double logarithmic scale according to:

$$\frac{da}{dN} = C \cdot \Delta \mathrm{CTOD}^{m}, \tag{1}$$

where C and m are material constants.[26–28] Pippan et al[29] suggested that the relationship between CGR and ΔCTOD also exists in small crack growth with slight variation from the linear trend. On the other hand, it is essential to note that experimental investigations on CGR and ΔCTOD relationship for small fatigue cracks are still in infancy.

Until recently, the CTOD has been measured using stereo imaging,[30,31] scanning electron microscopy,[32–34] and optical microscopy.[26] Although achieving accurate results close to the crack-tip, the measurements are usually limited to a few selected crack lengths because of experimental limitations.[35] With recent developments in contactless measurement techniques, such as digital image correlation (DIC),[36–38] the measurement process can be optimized, enabling high sample rate and full-field displacements. DIC has been used to investigate both long and microstructurally small fatigue cracks emphasizing the early-stage crack initiation, strain accumulation, and its dependence on microstructure.[39–42] The sub-micron strain measurements using SEM-DIC have shown that the strain is accumulated in the form of strain bands and that the grain boundaries have a role in the capability of transmitting or blocking slip.[43,44] Moreover, Abuzaid et al[38] observed several strain localizations that were prominent on one side of the grain boundary, while the adjacent grain showed little strain accumulation. The behavior was associated with the shielding effect of the grain boundary, which acted as a barrier for slip transmission. However, experimental studies have shown contrasting conclusions on grain boundaries' effect and their role in small fatigue crack growth.[45–48] For example, fluctuating crack growth has also been observed in single-crystal materials,[49] which indicates that other

mechanisms might also play a role in the growth of small fatigue cracks.

The recent studies by Gallo et al[41] and Malitckii et al[50] investigated the early-stage crack-tip interaction with local microstructural features and the accumulated shear strain localizations. These researchers observed retardation in the crack growth as the crack-tip would approach the shear strain localization (due to local hardening) and an increase in CGR as the crack-tip bypassed the localization through macroscopic cross-slip. It was concluded that at an early stage, the interaction of several elements developing during the fatigue process across several length scales influences the small fatigue crack growth (e.g., microstructural deformation patterns, accumulated shear strain). However, experimental investigation of the relationship between CGR and the local crack driving force was left as future work.

The objective of the current work is to study the behavior of microstructurally small fatigue cracks by performing high-resolution DIC measurements. The measurements provide insights into the critical aspects of small fatigue crack growth mechanisms influencing CGR and ΔCTOD, and should be considered in developing reliable growth models in the future. Thus, the work aims to fulfill the lack of systematic and high sample-rate ΔCTOD measurements that cover crack growth over multiple grains and grain boundaries and is not limited to a few selected crack lengths. This study focuses on the polycrystal metallic material with a body-centered cubic crystal structure widely used in various engineering applications.

It should be noted that several samples and tests were realized showing similar conclusions in terms of strain localization and crack growth rate behavior; among those, two representative samples were selected for further study of CTOD and presented in the current paper for the sake of brevity.

2 | MATERIAL AND METHODS

2.1 | Material and sample geometry

Fatigue tests were conducted on a ferritic 18% chromium stainless steel (ASTM UNS S43940), which chemical composition is shown in Table 1. This steel was selected due to its suitability for the annealing process without extensive formation of carbides.[51,52] To realise high-resolution DIC measurements in the sub-grain level, the grain size of the parent material was increased by annealing at 1100°C in a nitrogen atmosphere for 1 hour and quenched in water. The yield strength σ_{ys} of 300 MPa and ultimate strength σ_{uts} of 440 MPa were measured by tensile testing at a constant strain rate of 10^{-4} s^{-1} for the annealed steel (see Figure 1A). The volume-weighted grain size distribution, measured using the point-sampled intercept length method by Lehto et al,[53–55] is illustrated in Figure 1B. The annealing process increased the volume-weighted grain size to $d_v = 224$ μm.

The annealed steel was machined and ground on both surfaces to reach a 1 mm total thickness. Two single-edge notched tension specimens (SENT), namely *Specimen A* and *Specimen B*, were manufactured using electrical discharge machining (EDM); a schematic representation of the specimen geometry is illustrated in Figure 1C. Both surfaces of the specimens were polished to EBSD quality before the experiments according to standard procedures and finalized by colloidal silica polishing in a vibratory polisher to minimize the deformation induced by the specimen preparation process; see.[41]

To enable an accurate overlay of data from EBSD and DIC measurements, eight Vickers micro-indentation markers were placed on both surfaces of the specimens. The microstructure of the specimens was characterized by electron-backscatter diffraction (EBSD) using Zeiss Ultra 55 field emission SEM equipped with a Nordlys F + EBSD detector and Channel 5 software from Oxford Instruments. The acceleration voltage was set to 20 kV at a working distance of approximately 20 mm. The analyses were conducted with a step size of 2–5 μm. EBSD data were post-processed using the MTEX toolbox.[56,57] The Vickers micro-indentations were used to correct the drift-induced trapezoidal distortion in the EBSD data by skewing and scaling the orientation and grain boundary images.[58]

A silicon stamp was used to apply an optimized speckle pattern for high-resolution DIC analyses with a characteristic speckle size of 10 μm.[59] The speckle pattern was applied only to one surface of the specimens, called the *primary surface*, for further reference. The specimens' secondary surface (without speckle pattern) was left in a polished state and used to monitor crack length only, enabling further comparison between crack growth on opposite surfaces.

TABLE 1 Chemical composition of a ferritic 18% chromium stainless steel, wt.%.

C	Si	Mn	P	Cr	Mo	Nb	Ni	Ti	Cu	Al	As	Co	Sn	V	W
0.014	0.61	0.42	0.03	17.7	0.024	0.393	0.18	0.138	0.118	0.025	0.007	0.18	0.007	0.055	0.037

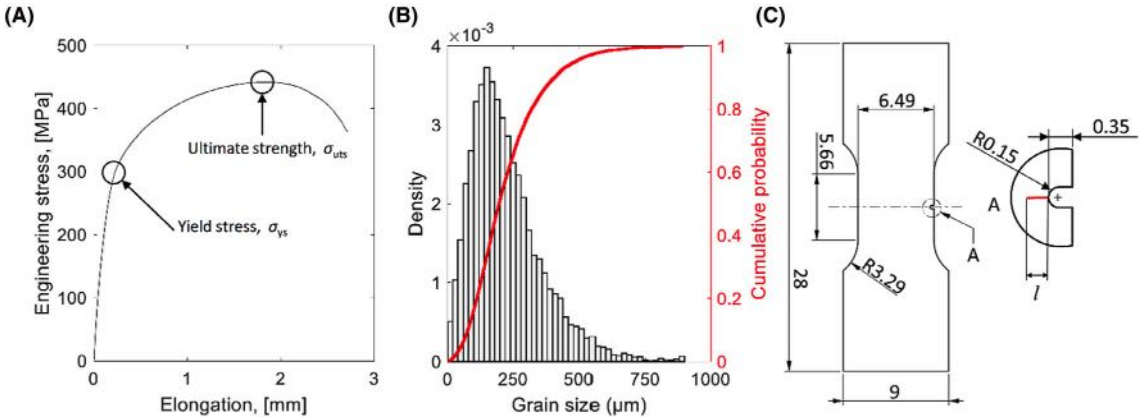

FIGURE 1 A) CERT stress-elongation curve, B) volume-weighted grain size distribution, and C) schematic of specimen used in the experimental tests (units in mm). [Colour figure can be viewed at wileyonlinelibrary.com]

As stated previously, two specimens were realized according to the procedures illustrated above, namely Specimen A and Specimen B. Specimen A was left in a "notched" state. A pre-crack of 36 μm (length l in Figure 1C) was realized on Specimen B to confirm crack-grown equality through specimen thickness at a very early stage. The pre-crack was realized using uniaxial cyclic loading with $\sigma_{max} = 240$ MPa, load ratio $R = -0.16$, and a test frequency of 10 Hz. Approximately 10,000 cycles were required to produce the pre-crack. A negative load ratio was used to increase the applied stress range without increasing the σ_{max}. Otherwise, pre-cracking would have required millions of load cycles with load ratio of $R = 0.1$, not being feasible since inspection for pre-crack detection is done every 1,000 cycles. In addition, the maximum stress σ_{max} would have exceeded the value used in subsequent fatigue tests (i.e. 250 MPa), resulting in monotonic loading-induced plasticity.

To ensure that the considered crack was outside the EDM-damaged layer and notch-tip plasticity affected region at the notch root, the subsequent analyses on CGR and ΔCTOD were started at a crack length of 60 μm. This value is determined based on experimental evidence of the extension of the damaged layer and the plastic region.[41]

2.2 | Fatigue experiments

The load-controlled fatigue tests were carried out at room temperature using a load ratio R of 0.1 and a loading frequency of 10 Hz. The applied load range on the net cross-section for Specimen A was $\Delta\sigma = 216$ MPa ($\sigma_{max} = 240$ MPa), and for Specimen B was $\Delta\sigma = 225$ MPa ($\sigma_{max} = 250$ MPa). It should be noted that there was no relevant temperature increase detected in the specimen at the given loading frequency and that tests were stopped at a maximum extension of 1.5 mm.

During fatigue testing, images were captured on both specimen surfaces using a dual-microscope setup illustrated schematically in Figure 2.[60] The primary surface was monitored by an optical microscope equipped with a 16 × Precision Zoom Lens and a digital camera with a 12MP resolution. The region of interest (ROI) of Specimen A was 2.1 mm × 1.6 mm with a spatial resolution of 0.79 μm/px. The ROI of Specimen B was 2.9 mm × 2.2 mm with a spatial resolution of 1.09 μm/px. The secondary surface was monitored by an optical microscope with a 4.5 × Precision Zoom Lens and a digital camera with a 12MP resolution. The ROIs for the secondary surface are the same as those reported above, but due to cropping from a larger field of view, the spatial resolutions were 1.07 μm/px and 1.63 μm/px for Specimen A and B, respectively.

Images were captured at maximum and minimum load levels during the unloading of the specimen with varying *acquisition intervals* during temporary constant load-holding periods of 5 s. For Specimen A, the acquisition interval varied from 5,000 (early crack propagation stage) to 500 cycles (late crack propagation stage). For Specimen B, images were taken every 500 cycles. From all images captured, a selection of frames was selected/extracted for the analyses with the following larger intervals: 10,000–1,000 cycles for Specimen A; 2,500–1,000 cycles for Specimen B. These varying *analysis intervals* were defined and adjusted based on the smallest observable crack growth increment (see also[60]).

The DIC analyses were performed using the commercial LaVision software (DaVis 8.3.1) on the ROIs defined earlier. Raw images of the primary surface were processed with a least-squares matching algorithm and small deformations assumption. Images captured at 5,000 and

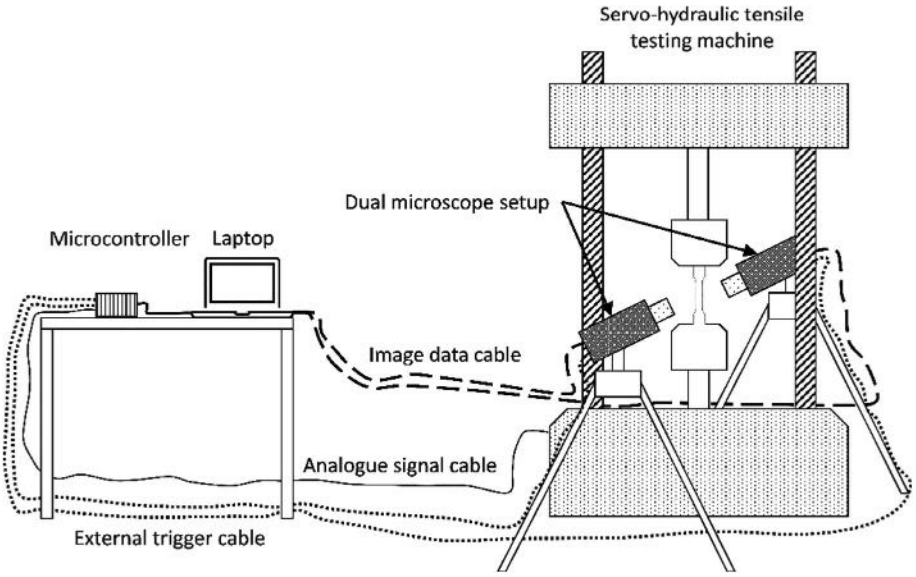

FIGURE 2 Schematic of the experimental setup.

500 load cycles (at maximum load level) were used as reference images for Specimen A and Specimen B, respectively. Specimens were analyzed with the same (within pixel size accuracy) subset size of 37 × 37 μm^2 and a step size of 7.5 μm. The subset size was 1/6th of the volume-weighted grain size and enabled full-field displacement measurements inside the grains. For the sake of clarity, ΔCTOD values were defined by the images at the maximum and minimum load levels of the selected cycle, while the accumulated shear strain was determined from images captured at the beginning of the test and the maximum load level of the selected cycle.

2.3 | Crack length and ΔCTOD measurements

The crack-tip location was determined from the high-resolution images by using a MATLAB program designed by the authors; for more details see reference.[60] This tool enables several functionalities to support accurate detection of the crack-tip from the microscopic images. For example, it provides different color scales and maps to control the image's contrast at the crack-tip. This methodology provided a really accurate visual inspection of the images and an accurate determination of the crack-tip. The crack length for both surfaces of the specimens was determined from microscopic images by performing the manual measurement series 10 times for the *analysis intervals* defined in the previous section. The mean crack length and its standard deviation were then calculated. One individual measurement falls in the 95% confidence interval, ± 2 standard deviation, i.e. ± 4.9 μm.[60] Based on the defined mean crack length, the crack growth rate was evaluated using the incremental polynomial method on sets of seven successive data points, according to ASTM E647-15.[61] In all subsequent analyses, the fitted values of crack size from the aforementioned local polynomial method are considered the effective crack lengths.[61] The local polynomial method permits to clearly differentiate between physically inherent variability of small-crack growth rate from variability related to the measurement errors.

For obtained crack lengths corresponding to a given number of cycles, the ΔCTOD is defined by comparing the DIC image at the maximum load (i.e., reference) with the image at the minimum load. The CTOD at the minimum and maximum load levels are defined based on the distance between upper and lower crack edges identified by a crack-edge detection algorithm. The working principles of the algorithm are presented in Figure 3A and are explained in more detail in Ref.[60] The measurement distance for CTOD from the crack-tip was defined based on analyzing the cyclic crack opening displacement (ΔCOD). In the analyses, ΔCOD was measured throughout the crack path and analyzed as a function of √r for all measured crack lengths (see Figure 4). For a distance r behind the crack-tip smaller than 50 μm (i.e. √r ≈ 0.2 √mm in Figure 4) elastic–plastic deformations and DIC subsets offset from crack surface[36,40] lead to a deviation from the expected linear behavior. Therefore, the ΔCTOD was measured at r = 50 μm behind the crack-tip by calculating the change in the vertical displacement between maximum and minimum load levels (see Figure 3B). The vertical (V) displacement is the displacement in loading direction (y-coordinate direction in Figure 3).

The incremental accumulation of maximum shear strain, as defined in,[40] was analyzed by comparing subsequent DIC images to the reference image taken at the

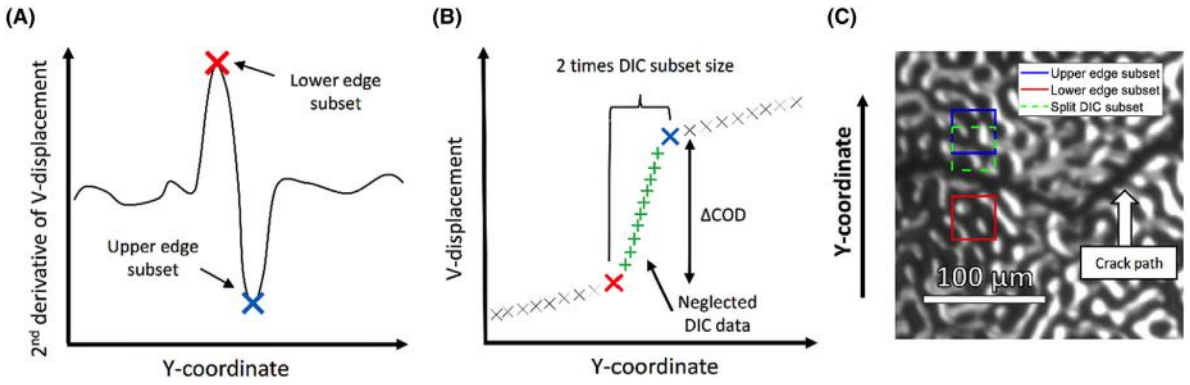

FIGURE 3 A) Crack edge definition by crack-edge detection algorithm, B) illustration of detected crack edges and neglected DIC data, and C) illustration of subsets in crack path's vicinity. [Colour figure can be viewed at wileyonlinelibrary.com]

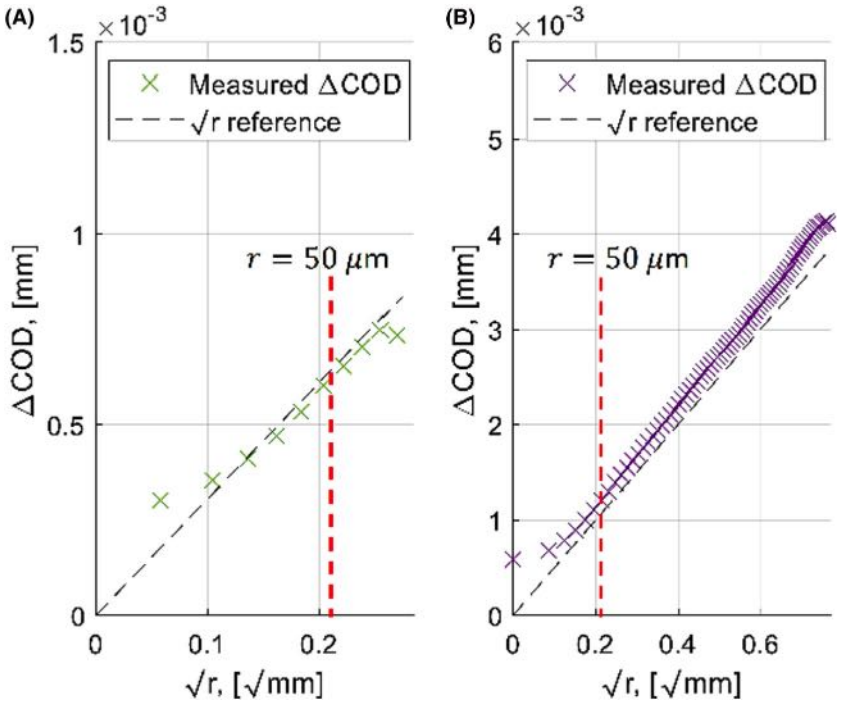

FIGURE 4 An example of measured crack opening displacement range ΔCOD vs. distance from the crack-tip (√r) at A) $l = 0.08$ mm, and B) $l = 0.60$ mm, where l is the crack length stemming from the notch root. [Colour figure can be viewed at wileyonlinelibrary.com]

beginning of the test. The accumulated maximum shear strain was plotted on top of the grain boundary map (based on EBSD data) using the Vickers micro-indentations as reference points for the alignment. The most significant shear strain localizations were studied using virtual strain gauges (VSGs). The VSGs measured the maximum shear strain averaged over 3 × 3 DIC adjacent interrogation points (approximately an area of 51 × 51 μm^2), and thus called the average accumulated maximum shear strain. In general, displacements for a single measurement point are derived in interrogation points that are centered in the subset. Adjacent interrogation points are then located within step size, leading to overlapping subsets. Near crack edges or other critical features, large overlap of adjacent subsets is recommended (80% overlap in the current study).

3 | RESULTS

3.1 | Crack growth behavior

The measured crack lengths of both specimens and on different surfaces are shown in Figure 5A. The fatigue tests were stopped at a maximum extension of 1.5 mm, i.e. the number of cycles to failure was approximately 656,500 and 332,500 for Specimen A and B, respectively. Crack initiation on Specimen A's primary surface was first observed after 65,000 cycles. On the secondary surface, the crack falls behind throughout test, as illustrated in Figure 5C. In the case of Specimen B, the crack-length observed on the primary surface was consistently shorter than that observed on the secondary surface. Due to pre-crack in Specimen B, this phenomenon is

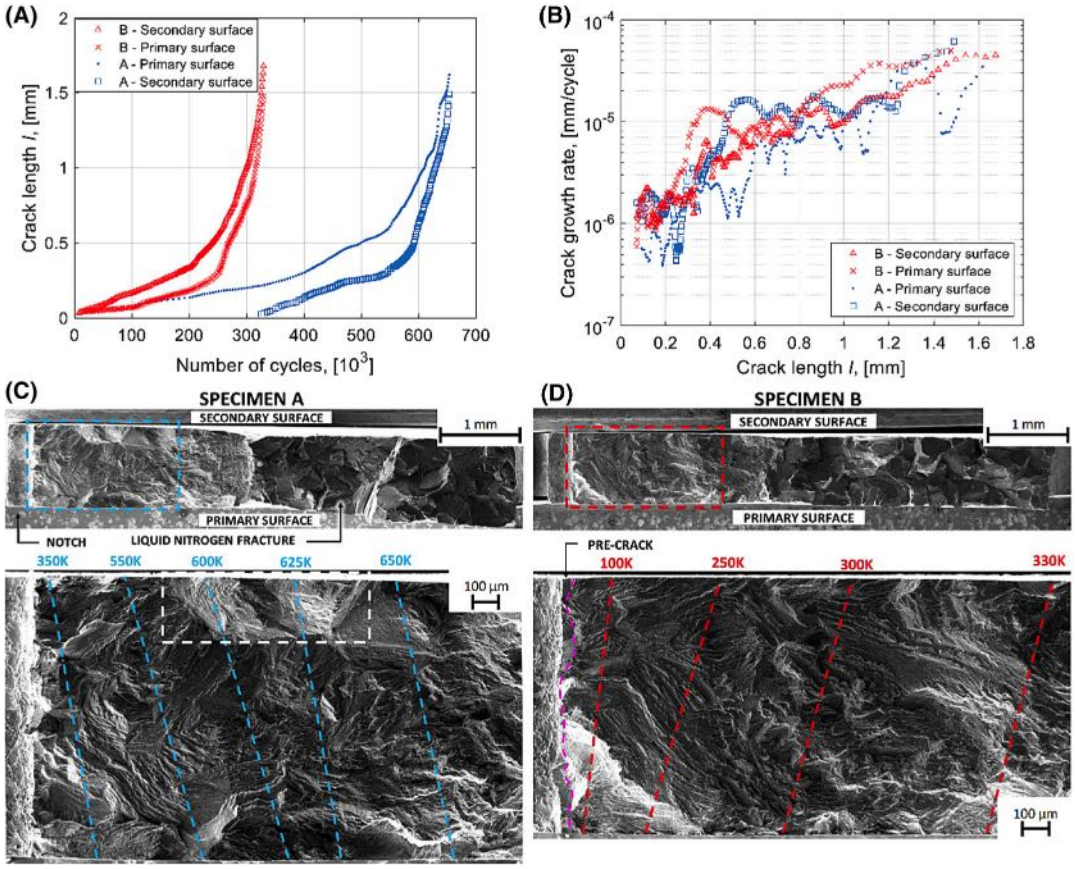

FIGURE 5 A) Crack length l vs. number of cycles, and B) crack growth rate vs. crack length l. SEM images of fracture surfaces of C) Specimen A and D) Specimen B. l is the physical crack length stemming from the notch root. [Colour figure can be viewed at wileyonlinelibrary.com]

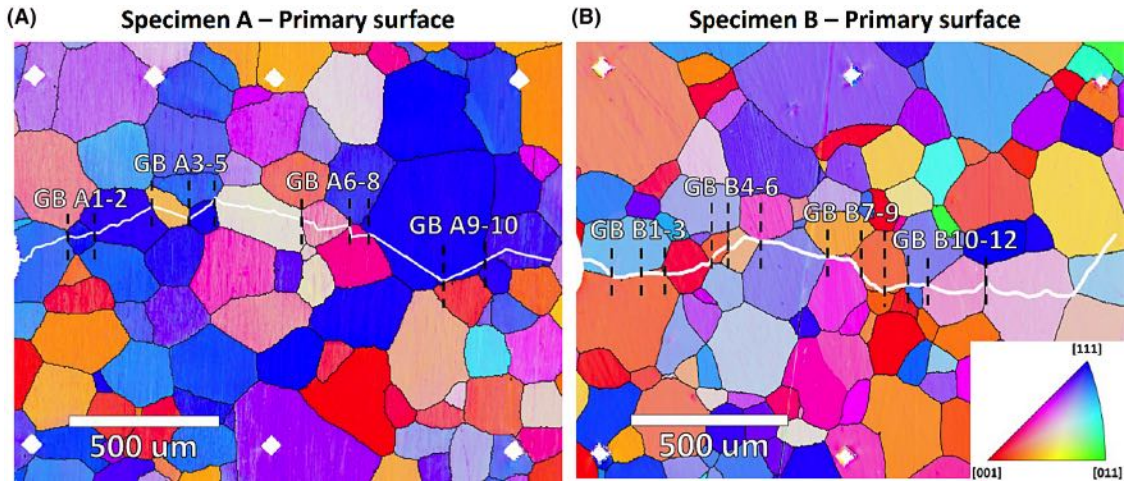

FIGURE 6 Inverse pole figure (IPF-Z) with IPF key of A) Specimen A and B) Specimen B. The observed crack path has been overlaid onto the orientation map based on the fiducial markers. The grain boundaries are marked based on the specimen name and grain number. For example, the first grain boundary of Specimen A is marked as GB A1. [Colour figure can be viewed at wileyonlinelibrary.com]

less pronounced at an early stage, but it becomes evident as the number of cycles increases. The dashed lines in Figure 5C–D illustrate approximately the location of the crack-tip as it is observed on different surfaces at the same number of cycles. Figure 5C–D also exhibits the fracture surfaces. The pre-cracking zone on Specimen B

is visible as a flat fracture surface, indicated by the dashed purple line (Figure 5D), after which a distinct change in fracture surface morphology was observed. The crack surface was faceted both at specimen surfaces and interior. The fracture surface of Specimen B was relatively flat, whereas the Specimen A had more evident inclined regions, as highlighted by the white rectangle in Figure 5C. Despite the crack front is not uniform because of local microstructural differences, the fracture surfaces did not show evident signs of tunneling. Figure 5B shows the CGR on opposite surfaces of the specimens. The CGR of specimens shows alternating trends with clear peaks and valleys. The corresponding crack growth path, grain boundaries and orientations are shown in Figure 6. The fatigue crack propagated via transgranular fracture, crossing multiple grain boundaries (GBs) and with several microscopic growth direction changes. This variation in CGR will be discussed after the analysis of accumulated maximum shear strains since it plays a role in fatigue dagame process and crack growth.

3.2 | Shear strain accumulation

During the whole fatigue crack growth, the shear strain accumulation was observed to localize at high-angle grain boundaries, triple grain junctions, and inside single grains as shown in Figure 7. Figure 7 presents selected examples of the accumulated maximum shear strain on the grain boundary map for four different crack lengths ($l = 0.07$, 0.21, 0.30, and 0.38 mm). The crack path is highlighted with a purple line (solid and dashed), and the

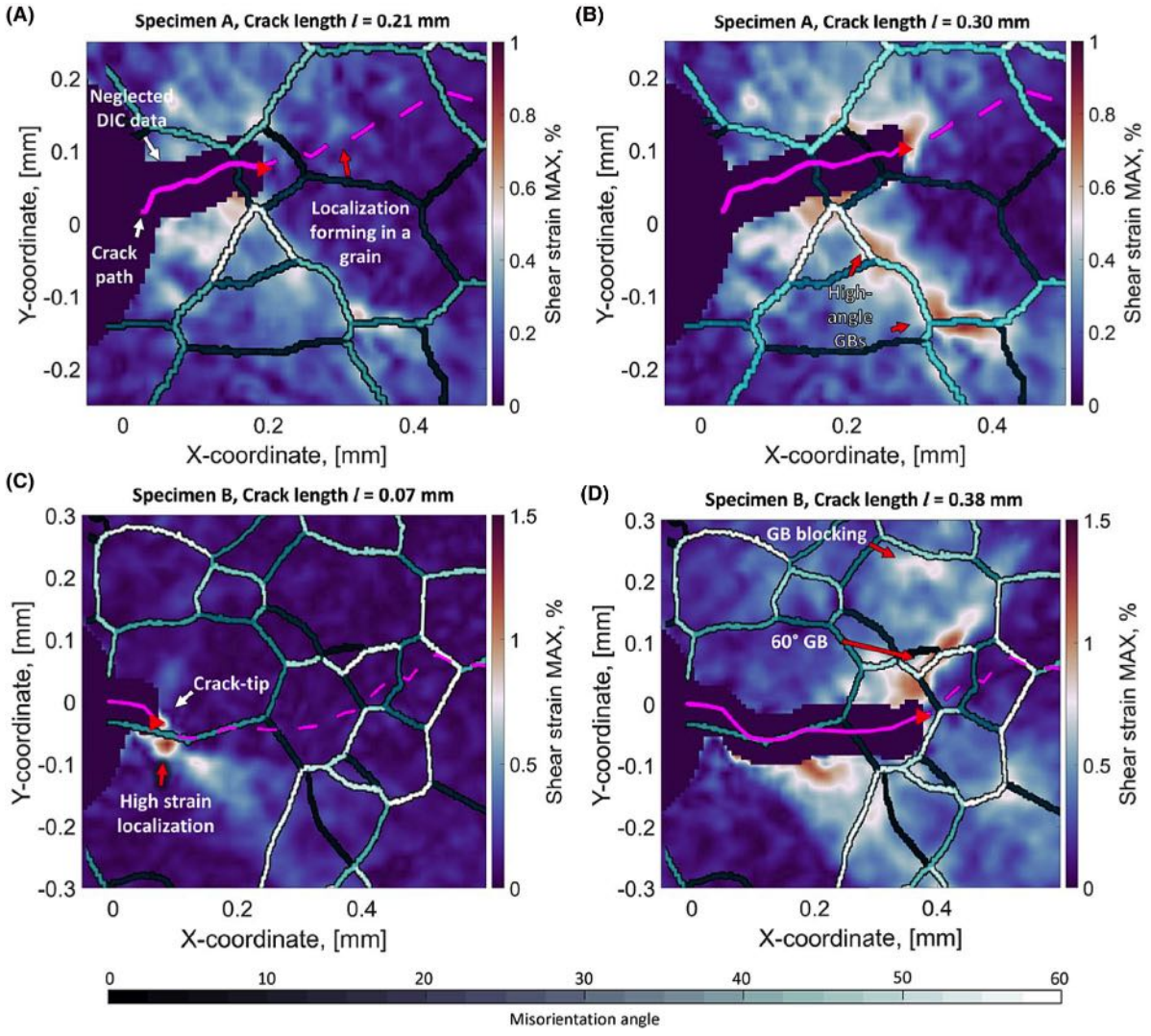

FIGURE 7 Accumulated maximum shear strain and grain boundary misorientation angle on A) specimen A, $l = 0.21$ mm, B) specimen A, $l = 0.30$ mm, C) specimen B, $l = 0.07$ mm, and D) specimen B, $l = 0.38$ mm, where l is crack length stemming from the notch root. The white arrows indicate crack-path related features, and the red arrows indicate features related to the strain localizations and grain boundaries. [Colour figure can be viewed at wileyonlinelibrary.com]

crack-tip location is indicated by a red triangle. The black area surrounding the crack path represents the subsets split by the physical crack that was neglected from the analyses (see also Figure 3B–C). Figure 7A–B shows the strain localization for Specimen A. In this case, the shear strain was observed to accumulate inside a single grain up to 0.2 mm ahead of the crack-tip, which is relatively far considering the current crack length (0.21 mm in Figure 7A). Figure 7C and Figure 7D shows the examples for Specimen B with crack length of l=0.07 and

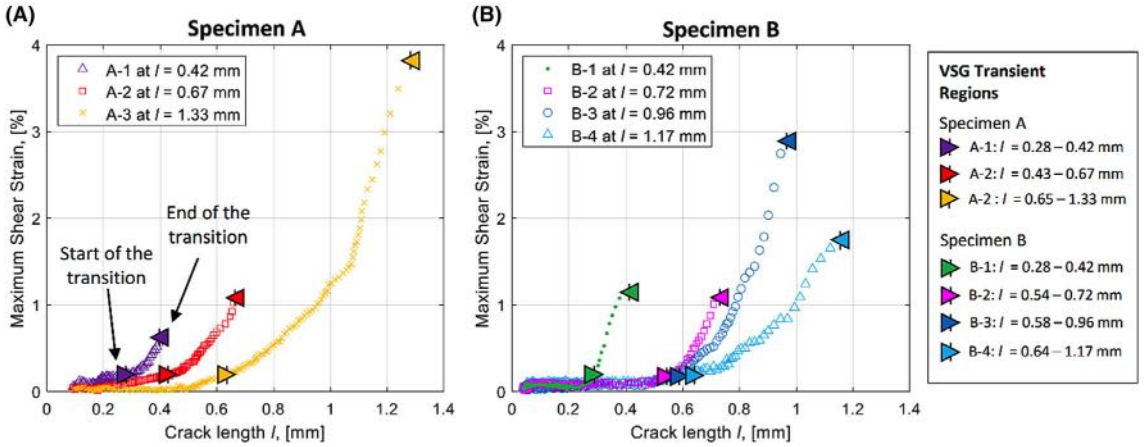

FIGURE 8 Shear strain accumulation at regions monitored by virtual strain gauges on A) Specimen A and B) Specimen B. Start and stop of transient regions in strain accumulation are reported by triangles for different crack lengths l, stemming from the notch root. [Colour figure can be viewed at wileyonlinelibrary.com]

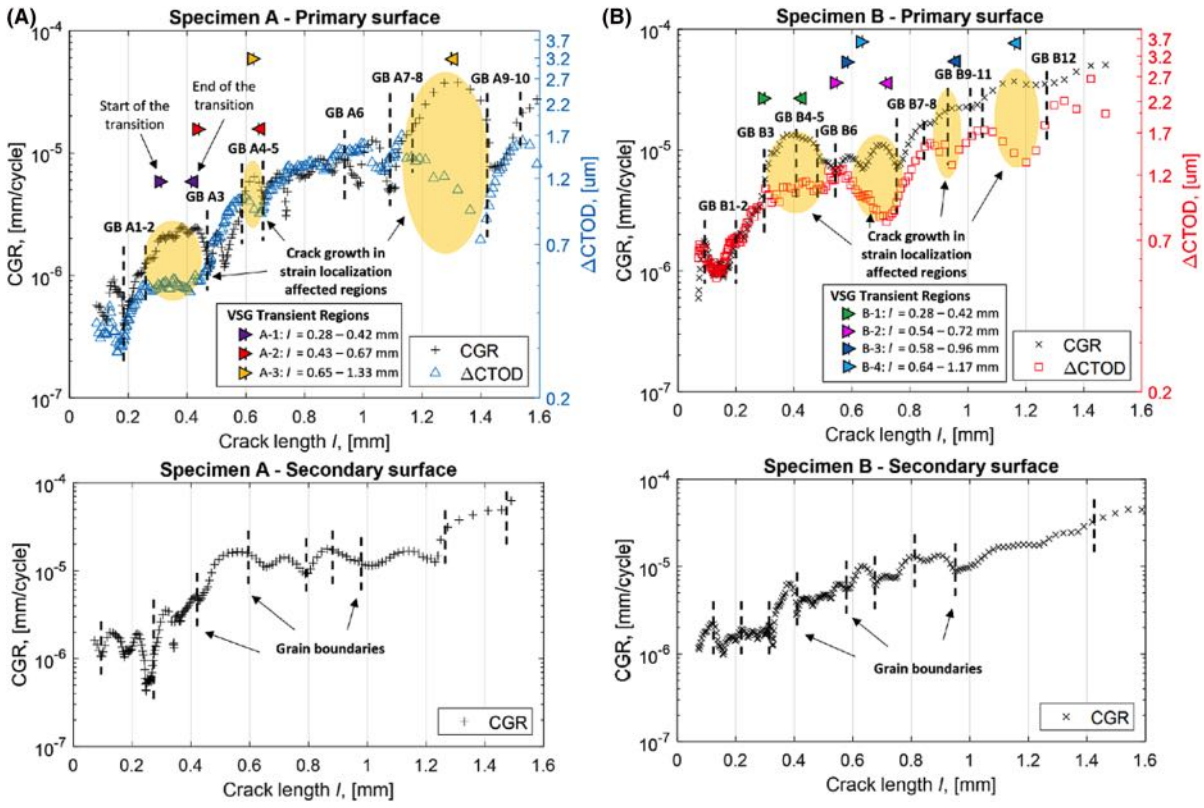

FIGURE 9 CGR and ΔCTOD with respect to crack length l stemming from the notch root on A) specimen A and B) specimen B. The regions affected by strain localizations are highlighted with yellow ellipses and the transient region in strain accumulation are pointed by arrows. [Colour figure can be viewed at wileyonlinelibrary.com]

0.38 mm. These examples show the strain localization for high-angle grain boundaries and triple-grain junctions. It is also worth mentioning that crack-tip was observed to preferentially grow always in the direction of the higher maximum shear strain (see the purple dashed line in Figure 7C–D).

The average accumulated maximum shear strain, measured by VSG is displayed in Figure 8 against the crack length. It is worth noticing that VSG is located always ahead of the growing crack-tip, and thus representing the behavior of shear strain accumulation before crack tip reaches the VSG measurement point. The VSGs nomenclature in Figure 8 reports the specimen name, the VSGs number, and its location in terms of crack length l, for instance, VSG A-1 at $l = 0.42$ mm. For all measured VSGs, the average accumulated maximum shear strain exhibits low values of deformation with almost a constant trend at the beginning of the experiments. As the crack grew and cyclic damage was accumulated ahead of the crack-tip, a sudden steep increment in the maximum shear strain was observed, representing the starting point of shear strain accumulation. The strain localization continues until crack-tip reaches the localization point and the shear strain its maximum value. This transient region of strain localization process (steep increment of maximum shear strain) is marked within triangles in Figure 8. It is worth noticing that the shear strain was accumulated far away from the crack-tip, even up to two times the physical crack length. For instance, the transient region in VSG A-3 started as the crack-tip was approximately 0.6 mm away from the VSG. The distance is significantly larger than the volume-weighted grain size $d_v = 224$ μm.

3.3 | Crack growth rate – ΔCTOD relation

The crack growth rate and ΔCTOD as a function of crack length are displayed in Figure 9. Changes in crack growth rate and ΔCTOD were observed both at grain boundaries and within the grains, such as between GB B6–7 in Figure 9B. Generally, the changes in ΔCTOD slightly preceded the changes in the crack growth rate (see Figure 9B, GB B1–2). Both crack growth rate and ΔCTOD increase or decrease at some grain boundaries, (see Figure 9A–B, GB A1 and GB B1). Despite these similarities, there were evident regions where ΔCTOD and CGR had unexpected opposing behavior; these are highlighted by yellow ellipses in Figure 9. The anomalous behavior is also visible in Figure 10, where the crack growth rate is given as a function of ΔCTOD on a double logarithmic scale. A power law curve was fitted to the experimental data according to ASTM E647–15.[61] The

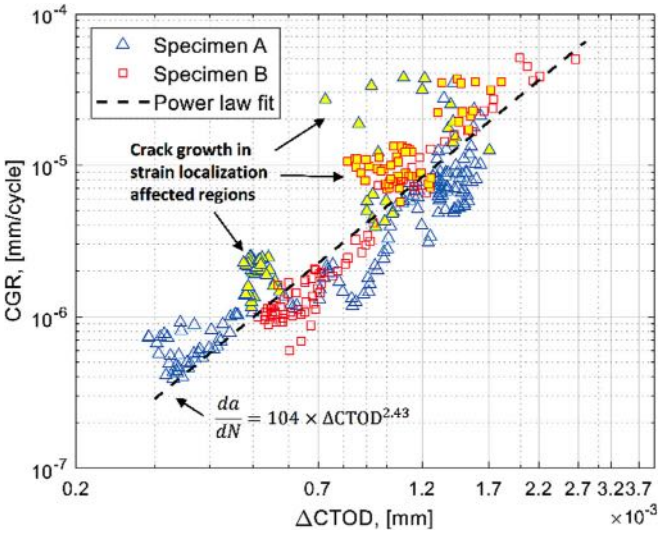

FIGURE 10 Crack growth rate vs. ΔCTOD, primary surface. Strain localization-affected regions are highlighted in yellow. [Colour figure can be viewed at wileyonlinelibrary.com]

crack growth rate and ΔCTOD have mostly linear relationship on double logarithmic scale. The variation from this otherwise linear trend was observed mainly at the regions with high maximum shear strain accumulation, indicating the influence of the shear strain localization on crack behavior and thus, also crack driving force ΔCTOD.

3.4 | Strain localization effects on crack growth behavior

Figure 11 and Figure 12 illustrate the evolution of shear strain localizations ahead the crack-tip throughout the fatigue tests, and the regions where CGR and ΔCTOD had opposing behavior (see also Figure 10). Within those regions, the crack-tip grew along the border of accumulated strain localization zone. Such instances were observed at locations of VSG A-2 and A-3 (see Figure 11). Similar behavior was observed also at locations of VSG B-3 and B-4 in Figure 12. In all areas where opposing CGR – ΔCTOD behavior was observed, the crack-tip seemed to bypass a significant shear strain localization without entering the area directly. When the crack physically entered shear strain localization instead (see e.g., 60° GB A9 in Figure 11), the crack-tip showed decreased crack growth rate (see Figure 9A).

Figure 13A exhibits the fracture surface of Specimen A primary surface, between 1.05 and 1.55 mm crack lengths, where opposing CGR – ΔCTOD behavior and inhomogeneous strain distribution were observed. The fractography analyses showed a change in the crack

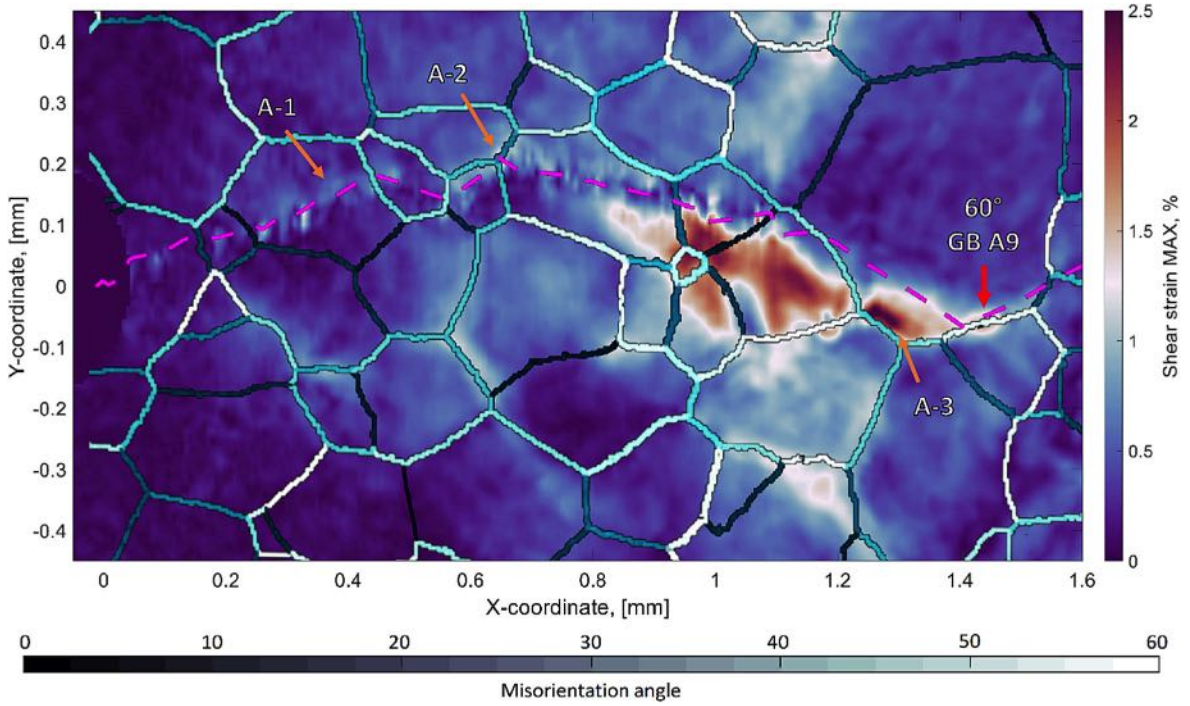

FIGURE 11 The evolution of shear strain localization and grain boundary misorientation angle on Specimen A. [Colour figure can be viewed at wileyonlinelibrary.com]

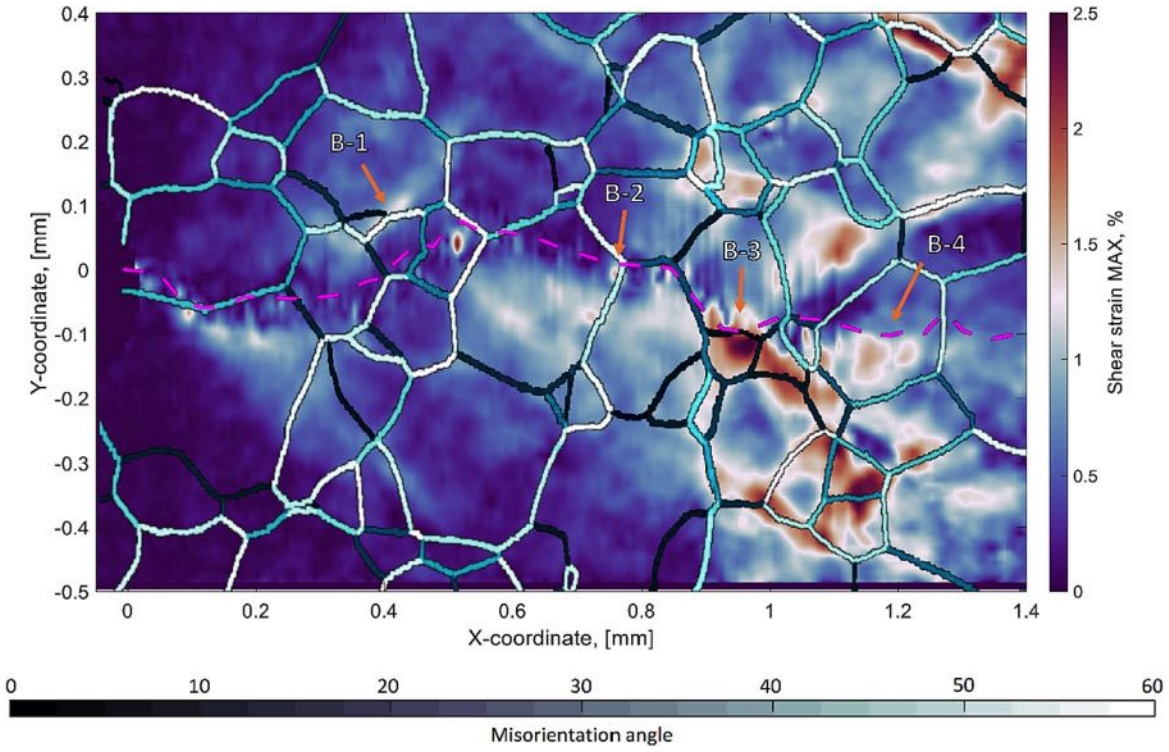

FIGURE 12 The evolution of shear strain localization and grain boundary misorientation angle on Specimen B. [Colour figure can be viewed at wileyonlinelibrary.com]

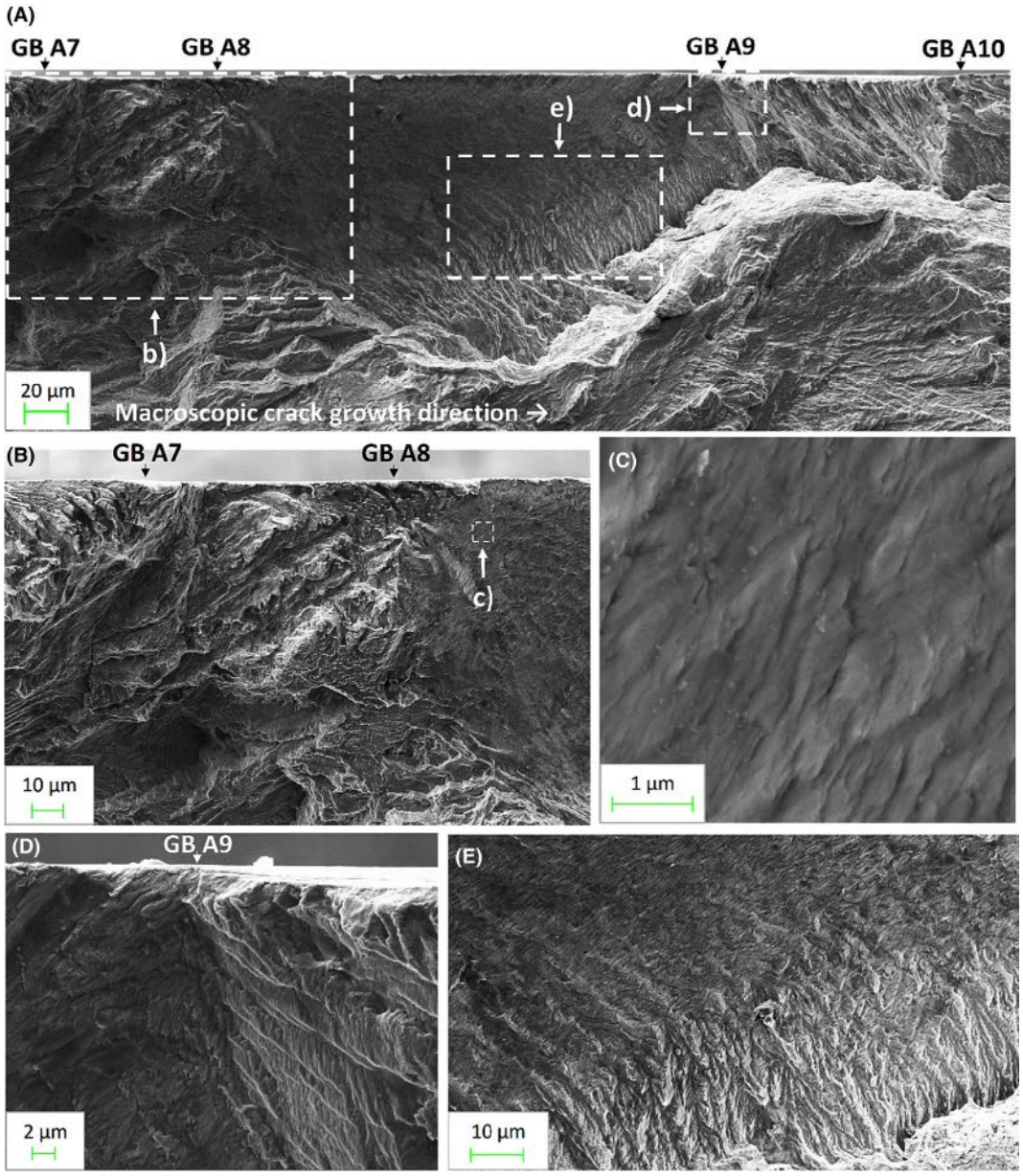

FIGURE 13 SEM fractography of Specimen A: A) between GB A7-10 B) near GB A9, C) transition in crack growth mechanism between GB A7-8, and D) and E) examples of gradual change in crack growth mechanism near shelf-like formation between GB A8-9. [Colour figure can be viewed at wileyonlinelibrary.com]

growth mechanism as the crack-tip propagated along the border between high-strain and low-strain areas between GB A8–9. The fracture surface preceding the accumulated strain area had a faceted fracture surface (see Figure 13B, preceding GB A8). After the crack-tip entered the accumulated strain area, the fracture surface shows no striations and has an appearance of fine deformation-induced sub-structure in Figure 13C, indicating fracture primarily by shearing.[62] In Figure 13D, A clear change in the crack growth mechanism was observed as the crack-tip deflected from GB A9 that seems to also confine the strain accumulation. The resulting fracture surface after GB A9 was faceted. The restriction of plasticity can be observed from the fracture surface in Figure 13E, where smooth fracture surface gradually changes to the faceted surface close to the shelf-like formation between GB A8-9. Specimen B showed similar characteristics and it is here omitted for the sake of brevity.

4 | DISCUSSION

The current work reveals that variation from the otherwise linear relationship between CGR and ΔCTOD on a

double logarithmic scale is due to the crack-tip bypassing a maximum shear strain accumulation area formed during cyclic loading. In some previous studies, the variation in the ΔCTOD was in general considered mainly as a scatter[29,63–65] due to large measurement intervals. The current work introduces high-resolution and high sample-rate experimental ΔCTOD measurements of a microstructurally small fatigue crack, growing from sub-grain level over multiple grains. The results show that the variation in the ΔCTOD and CGR is influenced by the shear strain localizations. Interaction with grain boundaries, therefore, is not the only factor affecting the CGR. Figure 11 illustrates that after the GB A4, the crack-tip bypassed a shear strain localization. While the crack-tip seems to initially grow towards the strain localizations, CGR may be hindered if the crack-tip physically enters that region (see e.g., localization at GB A9 shown in Figure 9A and Figure 11). In some cases, the crack-tip avoided the strain localizations by propagating along the border of such area. Such instance is highlighted by VSG B-3 in Figure 12, where the crack-tip propagated towards a low-angle (5°) grain boundary with high localized strain and smoothly changed its direction.

Figure 10 shows that there is mostly linear behavior between CGR and ΔCTOD on double logarithmic scale, while deviating behavior occurs primarily where the crack-tip propagated along the border of accumulated shear strain localization zones. A decrease in ΔCTOD was observed within aforementioned areas, which can be caused by the hardened region at the strain localizations.[41] This phenomenon affects the crack-tip opening and changes the crack growth mechanisms. Specifically, the growth in these locations is dominated by shear/tensile overload. Indeed, considerably inclined fracture surfaces were observed in the vicinity of these deviations. Pippan et al[66,67] also showed that local hardened regions and therefore local material mismatch affect both the crack-tip opening and the crack growth behavior. This study indicates that the effect of hardening region on CGR is higher than expected based on crack-tip opening displacement and thus commonly used relationship between CGR and ΔCTOD (Equation 1) breaks down if microstructurally small crack propagates through cyclic strain localization point, in which material properties are locally changed due to significant cyclic loading. In comparison to grain boundary, commonly used in microstructure sensitive fatigue model, the location of strain localization occurrence is more difficult to predict since it is affected by several factors such as grain size and orientation as well as the interaction of several grains. For instance, for Specimen A, the strain accumulation was observed especially in grains oriented in [111] direction pointing out of plane (see Figure 6), while Specimen B did not show a strong correlation between grain orientation and strain accumulation.

The results of the current work indicate that outside of the strain localization-affected regions, the ΔCTOD is a suitable local crack driving force. In strain localization-affected regions, the ΔCTOD does not characterize the behavior of microstructurally small fatigue crack. Models that are based on the local measurements of crack-tip opening should consider the effect of the strain localizations. It should be noted that current work considers only body-centered cubic ferritic stainless steel and further generalization requires additional study.

5 | CONCLUSIONS

The present work studied the relation between crack growth rate (CGR) and cyclic crack-tip opening displacement (ΔCTOD) of microstructurally small fatigue crack by using high-resolution digital image correlation with sub-grain level accuracy. A load-controlled fatigue experiments were carried out on small-scale specimens of 18% Cr stainless steel with body-centered cubic crystal structure. The high sample-rate measurement results were used to study the small crack behavior starting from sub-grain crack lengths up to seven times the volume-weighted grain size $d_v = 224\,\mu m$. EBSD and SEM fractography further complemented the analyses.

The following conclusions can be drawn:

- CGR and ΔCTOD have mostly a linear relationship on double logarithmic scale during the microstructurally small fatigue crack growth. Accumulation of maximum shear strain is systematically the cause of variation of this linear trend.
- Shear strain accumulation can occur both at grain boundaries and within the grains, and always ahead of the crack-tip.
- While the crack seems to grow towards strain localization, the CGR may be hindered by it if the crack directly penetrates the hardened region.
- When crack-tip is approaching a strain localization, the ΔCTOD always decreases due to the hardened region generated by the accumulation of the maximum shear strain.
- Fracture surface analyses revealed that in those areas where the crack is bypassing a shear strain accumulation, the crack would grow primarily along a single slip plane, thus CGR tends to increase.

Since strain accumulation at the crack-tip is also influenced by the grain orientation and grain size,[67] additional effort is required to analyze and consider the statistical

nature of the appearance, size, and magnitude of the shear strain localizations. This further development could contribute to define a reliable ΔCTOD for small fatigue crack and to support the development of valid crystal plasticity models able to include shear strain accumulation at high number of cycles.

AUTHOR CONTRIBUTIONS

Ilari Tillikainen: Methodology, Investigation, Formal analysis, Writing—Original draft; **Pasquale Gallo**: Conceptualization, Investigation, Writing—Original draft, Review, and Editing; Funding Acquisition; **Pauli Lehto**: Conceptualization, Investigation, Writing—Review and Editing; **Heikki Remes**: Conceptualization, Supervision, Writing—Review and Editing; Funding Acquisition.

ACKNOWLEDGMENTS

The present research was supported by the Academy of Finland (decisions nos. 298762 and 321244). We greatly appreciate the support provided by the laboratory technician Kim Widell and Dr. Evgenii Malitckii at Aalto University in planning and executing of the experimental tests, and by Manner Peik.

DATA AVAILABILITY STATEMENT

The data that support the findings of this study are available from the corresponding author upon reasonable request.

ORCID

Pasquale Gallo https://orcid.org/0000-0001-5742-8647
Pauli Lehto https://orcid.org/0000-0002-4689-6063
Heikki Remes https://orcid.org/0000-0002-5030-3494

REFERENCES

1. Liinalampi S, Remes H, Lehto P, Lillemäe I, Romanoff J, Porter D. Fatigue strength analysis of laser-hybrid welds in thin plate considering weld geometry in microscale. *Int J Fatigue*. 2016;87:143-152.
2. Remes H, Romanoff J, Lillemäe I, et al. Factors affecting the fatigue strength of thin-plates in large structures. *Int J Fatigue*. 2017;101:397-407.
3. Gallo P, Remes H, Romanoff J. Influence of crack tip plasticity on the slope of fatigue curves for laser stake-welded T-joints loaded under tension and bending. *Int J Fatigue*. 2017;99:125-136.
4. Remes H, Gallo P, Jelovica J, Romanoff J, Lehto P. Fatigue strength modelling of high-performing welded joints. *Int J Fatigue*. 2020;135:105555.
5. Main B, Jones M, Barter S. The practical need for short fatigue crack growth rate models. *Int J Fatigue*. 2021;142:105980.
6. Christ HJ, Fritzen CP, Köster P. Micromechanical modeling of short fatigue cracks. *Curr Opin Solid State Mater Sci*. 2014;18(4):205-211.
7. Hussain K. Short fatigue crack behaviour and analytical models: a review. *Eng Fract Mech*. 1997;58(4):327-354.
8. Wen W, Zhai T. Quantification of resistance of grain boundaries to short-fatigue crack growth in three dimensions in high-strength al alloys. *Metall Mater Trans a Phys Metall Mater Sci*. 2012;43(8):2743-2752.
9. Zhai T, Wilkinson AJ, Martin JW. A crystallographic mechanism for fatigue crack propagation through grain boundaries. *Acta Mater*. 2000;48(20):4917-4927.
10. Newman JC. Fatigue of engineered metallic materials using small-crack theory under constant- and variable-amplitude loading. *Fatigue Fract Eng Mater Struct*. 2021;44(10):2858-2870.
11. Tang K, Du Z, Ferro P, Berto F. Crack initiation and propagation from geometric microdefects: experiment and transition fatigue behavior. *Fatigue Fract Eng Mater Struct*. 2021;44(9):2323-2336.
12. Long DJ, Dunne FPE. On the mechanistic driving force for short fatigue crack path. *J Mech Phys Solids*. 2023;179:105368.
13. Castelluccio GM, Musinski WD, McDowell DL. Recent developments in assessing microstructure-sensitive early stage fatigue of polycrystals. *Curr Opin Solid State Mater Sci*. 2014;18(4):180-187.
14. Pearson S. Initiation of fatigue cracks in commercial aluminium alloys and the subsequent propagation of very short cracks. *Eng Fract Mech*. 1975;7(2):235-247.
15. Forsyth PJ. A two stage process of fatigue crack growth. In: *Crack propagation symposium*; 1961.
16. Forsyth PJ. Fatigue damage and crack growth in aluminium alloys. *Acta Metall*. 1963;11(7):703-715.
17. Vasudevan AK, Kujawski D. Implications of Δ K - R ratio in vacuum. *Fatigue Fract Eng Mater Struct*. 2022;45(6):1739-1750.
18. Brockman RA, Hoffman RM, Golden PJ, Musinski WD, Jha SK, John R. A computational framework for microstructural crack propagation. *Int J Fatigue*. 2021;152:106397.
19. Rovinelli A, Sangid MD, Proudhon H, Ludwig W. Using machine learning and a data-driven approach to identify the small fatigue crack driving force in polycrystalline materials. *Npj Comput Mater*. 2018;4(1):35.
20. Omar I, Khan M, Starr A. Compatibility and challenges in machine learning approach for structural crack assessment. *Struct Heal Monit*. 2022;21(5):147592172110613.
21. Jones R, Singh Raman RK, McMillan AJ. Crack growth: does microstructure play a role? *Eng Fract Mech*. 2018;187:190-210.
22. Wolf E. Fatigue crack closure under cyclic tension. *Eng Fract Mech*. 1970;2(1):37-45.
23. Tanaka K, Nakai Y, Yamashita M. Fatigue growth threshold of small cracks. *Int J Fract*. 1981;17(5):519-533.
24. Akiniwa Y, Tanaka K, Matsui E. Statistical characteristics of propagation of small fatigue cracks in smooth specimens of aluminium alloy 2024-T3. *Mater Sci Eng a*. 1988;104:105-115.
25. Donahue RJ, Clark HM, Atanmo P, Kumble R, McEvily AJ. Crack opening displacement and the rate of fatigue crack growth. *Int J Fract Mech*. 1972;8(2):209-219.
26. Tanaka K, Hoshide T, Yamada A, Taira S. Fatigue crack propagation in biaxial stress fields. *Fatigue Fract Eng Mater Struct*. 1979;2(2):181-194.
27. Castelluccio GM, McDowell DL. Assessment of small fatigue crack growth driving forces in single crystals with and without slip bands. *Int J Fract*. 2012;176(1):49-64.

28. Tanaka K, Hoshide T, Sakai N. Mechanics of fatigue crack propagation by crack-tip plastic blunting. *Eng Fract Mech*. 1984;19(5):805-825.
29. Pippan R, Zelger C, Gach E, Bichler C, Weinhandl H. On the mechanism of fatigue crack propagation in ductile metallic materials. *Fatigue Fract Eng Mater Struct*. 2011;34(1):1-16.
30. Lankford J, D D. In: Davidson D, Suresh S, eds. *Near-threshold crack tip strain and crack opening for large and small fatigue cracks*. Metallurgical Society of Aime; 1984.
31. Williams DR, Davidson DL, Lankford J. Fatigue-crack-tip plastic strains by the stereoimaging technique. *Exp Mech*. 1980; 20(4):134-139.
32. Morris WL. The noncontinuum crack tip deformation behavior of surface microcracks. *Metall Trans A*. 1980;11(7):1117-1123.
33. Halliday M. In situ SEM observations of the contrasting effects of an overload on small fatigue crack growth at two different load ratios in 2024-T351 aluminium alloy. *Int J Fatigue*. 1997; 19(4):273-282.
34. Andersson H. In-situ SEM study of fatigue crack growth behaviour in IN718. *Int J Fatigue*. 2004;26(3):211-219.
35. Larsen J, Jira J, Ravichandran K. Measurement of small cracks by photomicroscopy: experiments and analysis. In: Allison JE, ed. *Small-crack test methods*. ASTM International; 1992:57-80.
36. Pan B, Qian K, Xie H, Asundi A. Two-dimensional digital image correlation for in-plane displacement and strain measurement: a review. *Meas Sci Technol*. 2009;20(6):062001.
37. Tong J. Full-field characterisation of crack tip deformation and fatigue crack growth using digital image correlation—a review. *Fatigue Fract Eng Mater Struct*. 2018;41(9):1855-1869.
38. Abuzaid W, Sehitoglu H, Lambros J. Plastic strain localization and fatigue micro-crack formation in Hastelloy X. *Mater Sci Eng A*. 2013;561:507-519.
39. Carroll JD, Abuzaid W, Lambros J, Sehitoglu H. High resolution digital image correlation measurements of strain accumulation in fatigue crack growth. *Int J Fatigue*. 2013;57:140-150.
40. Jiang R, Pierron F, Octaviani S, Reed PAS. Characterisation of strain localisation processes during fatigue crack initiation and early crack propagation by SEM-DIC in an advanced disc alloy. *Mater Sci Eng a*. 2017;699:128-144.
41. Gallo P, Lehto P, Malitckii E, Remes H. Influence of microstructural deformation mechanisms and shear strain localisations on small fatigue crack growth in ferritic stainless steel. *Int J Fatigue*. 2022;163:107024.
42. Vasco-Olmo JM, Díaz FA, Neto DM, Sérgio ER, Antunes FV, James MN. Evaluation of small-scale yielding boundary using digital image correlation results. *Fatigue Fract Eng Mater Struct*. 2022;45(4):1276-1291.
43. Di Gioacchino F, Quinta da Fonseca J. Plastic strain mapping with sub-micron resolution using digital image correlation. *Exp Mech*. 2013;53(5):743-754.
44. Patriarca L, Abuzaid W, Sehitoglu H, Maier HJ. Slip transmission in bcc FeCr polycrystal. *Mater Sci Eng A*. 2013;588: 308-317.
45. Long M, Crooks R, Rack H. High-cycle fatigue performance of solution-treated metastable-β titanium alloys. *Acta Mater*. 1999; 47(2):661-669.
46. Schäf W, Marx M, Knorr AF. Influence of microstructural barriers on small fatigue crack growth in mild steel. *Int J Fatigue*. 2013;57:86-92.
47. Schaef W, Marx M, Vehoff H, Heckl A, Randelzhofer P. A 3-D view on the mechanisms of short fatigue cracks interacting with grain boundaries. *Acta Mater*. 2011;59(5):1849-1861.
48. Tokaji K, Ogawa T. The growth behaviour of microstructurally small fatigue cracks in metals. In: KJ MI, de los Rios ER, eds. *Short fatigue cracks*. Vol.13. ESIS Publication; 1992:85-99.
49. Zhang XP, Wang CH, Ye L, Mai YW. In situ investigation of small fatigue crack growth in poly-crystal and single-crystal aluminium alloys. *Fatigue Fract Eng Mater Struct*. 2002;25(2): 141-150.
50. Malitckii E, Remes H, Lehto P, Yagodzinskyy Y, Bossuyt S, Hänninen H. Strain accumulation during microstructurally small fatigue crack propagation in bcc Fe-Cr ferritic stainless steel. *Acta Mater*. 2018;144:51-59.
51. Malitckii E, Yagodzinskyy Y, Lehto P, Remes H, Romu J, Hänninen H. Hydrogen effects on mechanical properties of 18% Cr ferritic stainless steel. *Mater Sci Eng A*. 2017;700:331-337.
52. Malitckii E, Remes H, Lehto P, Bossuyt S. Full-field strain measurements for microstructurally small fatigue crack propagation using digital image correlation method. *J vis Exp*. 2019; (143). doi:10.3791/59134. PMID: 30735166.
53. Lehto P, Remes H, Saukkonen T, Hänninen H, Romanoff J. Influence of grain size distribution on the Hall–Petch relationship of welded structural steel. *Mater Sci Eng A*. 2014;592:28-39.
54. Lehto P, Romanoff J, Remes H, Sarikka T. Characterisation of local grain size variation of welded structural steel. *Weld World*. 2016;60(4):673-688.
55. Lehto P. *Measurement and visualisation of grain size variation using Matlab: point-sampled linear intercept length method*. 2021.
56. Lehto P. Adaptive domain misorientation approach for the EBSD measurement of deformation induced dislocation substructures. *Ultramicroscopy*. 2021;222:113203.
57. Lehto P. *EBSD measurement and visualisation of grain size variation: MTEX implementation for linear intercept length method*.
58. Sørensen BE, Hjelen J, Ånes HW, Breivik T. Recent features in EBSD, including new trapezoidal correction for multi-mapping. *IOP Conf Ser Mater Sci Eng*. 2020;891(1):012021.
59. Bossuyt S. Optimized patterns for digital image correlation. In: Jin H, Sciammarella C, Furlong C, Yoshida S, eds. *Imaging methods for novel materials and challenging applications*. Vol.3. New York, NY, Springer New York; 2013:239-248.
60. Tillikainen I, Lehto P, Malitckii E, Gallo P, Remes H. A novel method for measurements of microstructurally small fatigue crack growth using digital image correlation. In: *International conference on fracture and damage mechanics*; 2023. 020013.
61. ASTM E647-15e1. *Standard test method for measurement of fatigue crack growth rates*. ASTM International; 2015.
62. Li Z, Yang X, Tang A. A fracture criterion for prediction of fracture initiation of metal materials at various stress states for nuclear waste storage. *Sci Technol Nucl Install*. 2019;2019:1-14.
63. Schweizer C, Seifert T, Nieweg B, Von Hartrott P, Riedel H. Mechanisms and modelling of fatigue crack growth under combined low and high cycle fatigue loading. *Int J Fatigue*. 2011; 33(2):194-202.
64. Vasco-Olmo JM, Díaz Garrido FA, Antunes FV, James MN. Plastic CTOD as fatigue crack growth characterising parameter in 2024-T3 and 7050-T6 aluminium alloys using DIC. *Fatigue Fract Eng Mater Struct*. 2020;43(8):1719-1730.

65. Ktari A, Baccar M, Shah M, Haddar N, Ayedi HF, Rezai-Aria F. A crack propagation criterion based on ΔCTOD measured with 2D-digital image correlation technique. *Fatigue Fract Eng Mater Struct*. 2014;37(6):682-694.
66. Pippan R, Riemelmoser F. Fatigue of bimaterials. Investigation of the plastic mismatch in case of cracks perpendicular to the interface. *Comput Mater Sci*. 1998;13(1-3):108-116.
67. Pippan R, Flechsig K, Riemelmoser FO. Fatigue crack propagation behavior in the vicinity of an interface between materials with different yield stresses. *Mater Sci Eng A*. 2000;283(1-2):225-233.

How to cite this article: Tillikainen I, Gallo P, Lehto P, Remes H. Study of cyclic crack-tip opening displacement of microstructurally small fatigue crack using digital image correlation. *Fatigue Fract Eng Mater Struct*. 2023;1-16. doi:10.1111/ffe.14124